Probing the Cosmic X-ray Laboratory with the Chandra HETGS

K. A. Flanagan, C. R. Canizares, D. Dewey, A. Fredericks,
J. C. Houck, J.C. Lee, H. L. Marshall and M. L. Schattenburg

MIT Center for Space Research, 77 Massachusetts Ave., Cambridge, MA

ABSTRACT

The High Energy Transmission Grating Spectrometer (HETGS) on the *Chandra* X-ray Observatory is a powerful tool for studying the astrophysical properties of X-ray emitting objects. Emission and absorption lines and features can probe the physical properties of stellar winds, relativistic jets, supernova remnants (SNRs), active galactic nuclei and the intergalactic medium. The capabilities of this instrument are illustrated through highlights of HETGS science, with examples including the jet structure in SS433, a Doppler velocity map of SNR E0102-72, and evidence of abundance anomalies in the microquasar GRS1915+105.

Keywords: spectrometer, X-ray, grating, plasma, Doppler

1. INTRODUCTION

The *Chandra* X-ray Observatory was more than two decades in the making, with ambitious goals for its flight hardware and an equally ambitious calibration program. *Chandra* was placed in orbit three years ago, setting a new benchmark in X-ray astronomy imaging and spectroscopy. This paper presents a look at the High Energy Transmission Grating Spectrometer, illustrating its capabilities through recent science highlights from a variety of astrophysical sources.

The HETG consists of two independent sets of gratings with dispersion axes oriented at angles that differ by $\sim 10^\circ$. The medium energy gratings (MEG) cover an energy range of $0.4 - 5$ keV and have half the dispersion of the high energy gratings (HEG), which provide simultaneous coverage of the range $0.9 - 10$ keV. The gratings form an undispersed image at the pointing position (the zeroth order image) with *Chandra's* full spatial resolution, and with spectral information limited to the moderate resolution provided by the ACIS detector. The dispersed photons provide the high resolution spectrum. The different dispersion directions and two dispersion wavelength scales provide redundancy as well as a means of resolving spectral/spatial confusion problems associated with extended sources such as supernova remnants. Further details of the instrument can be found in Markert *et al.*[1], the Chandra Proposers' Guide[2], and at `http://space.mit.edu/HETG`.

2. SUPERNOVA REMNANT 1E0102-7219

The SNR 1E 0102.2-7219 (E0102), located in the Small Magellanic Cloud (SMC), is a well studied member of the oxygen-rich class of supernova remnants. As a class, oxygen-rich SNRs are believed to come from supernovae with massive progenitors, exhibit high velocities in their optical filaments, and often exhibit asymmetry. Images of E0102, such as the zeroth order grating image of Figure 3, show an almost classic, text-book SNR with a hotter outer ring identified with the forward shock surrounding a cooler, denser inner ring which is presumably the reverse-shocked stellar ejecta (Gaetz *et al.*[3]). Moderate resolution X-ray spectra have been obtained with ASCA (Hayashi *et al.*[4]) and XMM–Newton (Sasaki *et al.*[5]). A high resolution X-ray spectrum obtained with the Reflection Grating Spectrometer of XMM–Newton reveals a wealth of individual lines of C, O, Ne, Mg and Si (Rasmussen *et al.*[6]). Line ratios from these spectra confirm non-equilibrium ionization (NEI) conditions

Further author information: (Send correspondence to K.A.F.)
K.A.F.: E-mail: kaf@space.mit.edu, Telephone: 617 258 7324

X-Ray and Gamma-Ray Telescopes and Instruments for Astronomy, Joachim E. Trümper, Harvey D. Tananbaum, Editors, Proceedings of SPIE Vol. 4851 (2003)

consistent with an ionizing plasma in the low density limit, and provide temperature constraints for the OVII and Ne IX emitting plasma.

E0102 was observed with the *Chandra* High Energy Transmission Grating Spectrometer (HETGS) (Canizares *et al.*[7,8]) on September 29 and October 8, 1999. We present here some of the results obtained from the HETG spectrum. Further details can be found in Flanagan *et al.*[9,10,11], and Canizares *et al.*[12].

The sharply defined X-ray ring of the SNR and the high spatial/spectral resolution of the HETGS reveal the two-dimensional structure of this extended object in several prominent lines. These are clearly seen in the dispersed spectrum of Figure 1. Individual X-ray lines of oxygen, neon, magnesium and silicon are evident, echoing the sharp bright ring-and-spoke structure seen in the zeroth order. Notably weak are lines of highly ionized iron. This lack of strong iron lines is fortuitous, since the X-ray spectra of SNRs are commonly dominated (and complicated) by an "iron forest" of lines between 7 *Å* and 18 *Å*. The spatial and spectral signatures of E0102 make it a unique candidate for the HETG – bright, sharp spatial features arrayed in a narrow ring around a sparsely filled interior, combined with a spectrum dominated by a relatively small number of discrete lines. As a result, the HETG dispersed line images have only a small amount of overlap between them, enabling uncontaminated analysis of the individual lines.

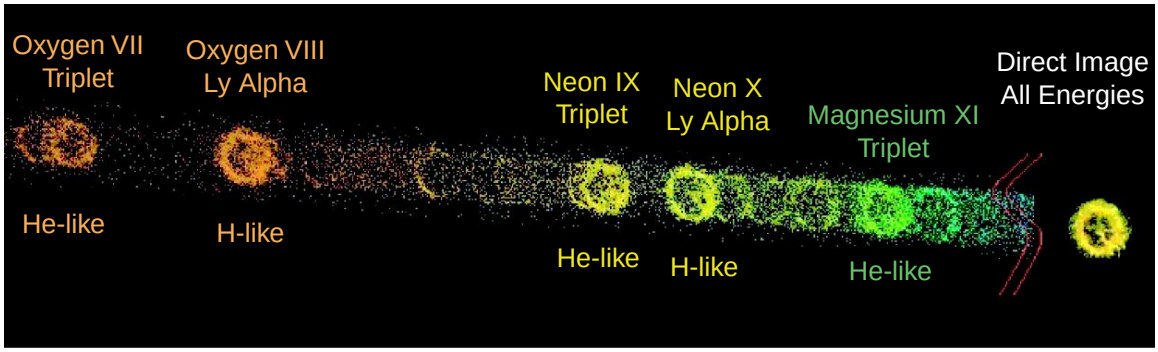

Figure 1. Dispersed high resolution spectrum of E0102. Shown here is a portion of the MEG -1 order, color coded to suggest the ACIS energy resolution. At right in the figure (with different intensity scaling) is the zeroth order, which combines all energies in an undispersed image. Images formed in the light of several strong X-ray emission lines are labeled. This figure is truncated and does not show the silicon. (Flanagan *et al.*[9])

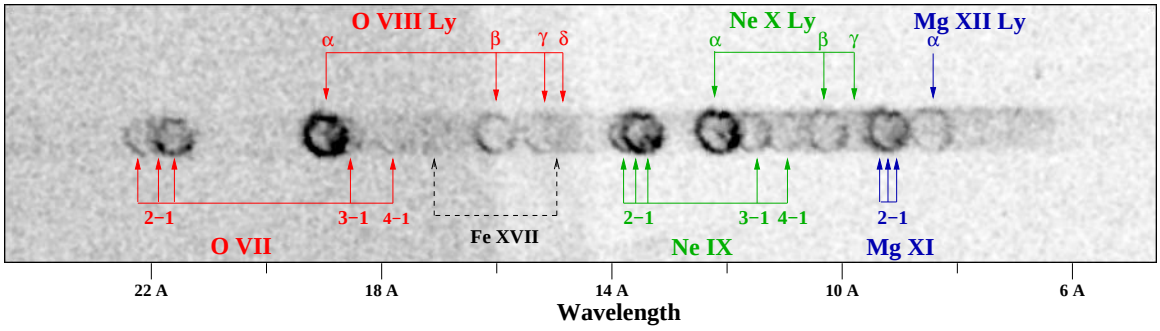

Figure 2. Lines identified in the HETG spectrum of E0102 arise from helium-like and hydrogen-like ionization stages of oxygen, neon, magnesium and silicon. Ratios of the fluxes of these lines allow conditions in the plasma to be sensitively explored. (Flanagan *et al.*[9])

2.1. Plasma Diagnostics

High resolution grating spectra provide a means of probing the plasmas by the use of individual X-ray lines. Flux ratios formed from different lines from the same element serve as particularly useful plasma diagnostics because

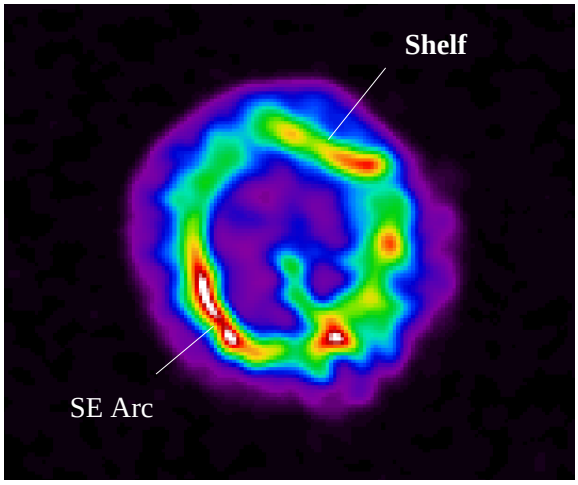

Figure 3. Zeroth-order (undispersed) image of E0102. Two bright regions are indicated: the linear "shelf" feature to the north, and the bright arc in the southeast. Edge profiles of these regions were used to measure the distance parameter plotted in Figure 5. The overall extent of the SNR is about 40 arcsec.

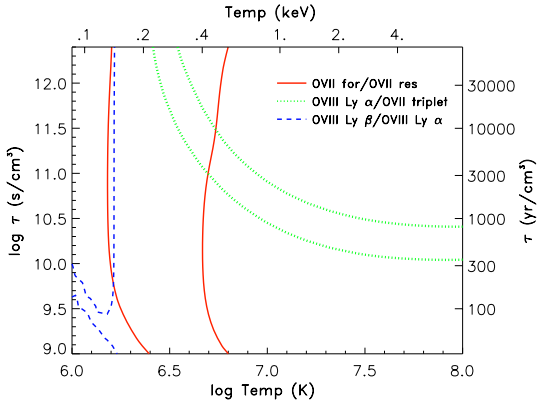

Figure 4. The 90% confidence contours are plotted for vpnshock model ratios among the brightest O VII and O VIII lines. The overlap region indicates the "allowed" range of temperature and ionization timescale that is compatible with the measurements.(Flanagan *et al.*[9])

they eliminate the impact of uncertainties in abundance or distance. If lines from the same ion are selected, dependence on the ionization fraction is eliminated. (This can provide, for example, a useful diagnostic for electron temperature or density.) Figure 2 shows many of the lines identified in the HETG spectrum of E0102. To illustrate this approach to plasma diagnostics, refer to Figure 4. We have calculated ratios of measured HETGS fluxes of lines corresponding to the n=2 to n=1 transitions of hydrogen-like (O VIII) and helium-like (O VII) oxygen. We assumed a model (Borkowski *et al.*[13]) for the shocked SNR plasma, and examined the range of parameters in that model that reproduces the flux ratios measured in the HETG spectrum. Since the evolution of the plasma is mediated by collisions, one of the parameters is the ionization timescale, τ, which is the product of elapsed time and electron density. The other parameter shown in the figure is the electron temperature. The overlap region in Figure 4, (i.e., $0.2 < T_e < 0.4$ keV and $\log \tau > 11.0$ s cm^{-3}) indicates the "allowed" range of temperature and ionization timescale that is compatible with the measurements under this model.

2.2. Ionization/Shock Structure

Direct images of E0102 by ACIS show OVII emission enhanced at the inner edge of the X-ray ring and the outer part enhanced in OVIII emission, suggesting progressive ionization by a "reverse shock" moving inward relative to the ejecta (Gaetz, *et al.*[3]). ACIS does not cleanly resolve X-ray lines from different ionization states, however, and this limits the analysis that can be done with direct images. In contrast, the HETG observation permits well resolved monochromatic line images. We measured the top and bottom edges of the bright ring images in the dispersed spectrum by extracting the intensity profiles along a segment perpendicular to the dispersion direction. (Doppler shifts affect the spectrum along the dispersion direction, so this analysis is restricted to regions of the SNR perpendicular to the dispersion direction.) An empirical model was used to fit the emission profile and localize the peak of the emission. The model assumed an expanding, partially filled shell inclined to the line-of-sight. To better fit the steep peak profile, the radial distribution was given a power law dependence. The analysis confirmed that for each element, the emission from hydrogen-like ionization stages peaks at a larger radius than the helium-like ionization stages (Flanagan *et al.*[11]), as expected from the propagation of the reverse shock.

Figure 5 shows the result of applying a simple model (Flanagan, *et al.*[9]). We assumed that the location of the SNR edge, defined by the peak of the radial emission profile, correlates with the ionization timescale, τ.

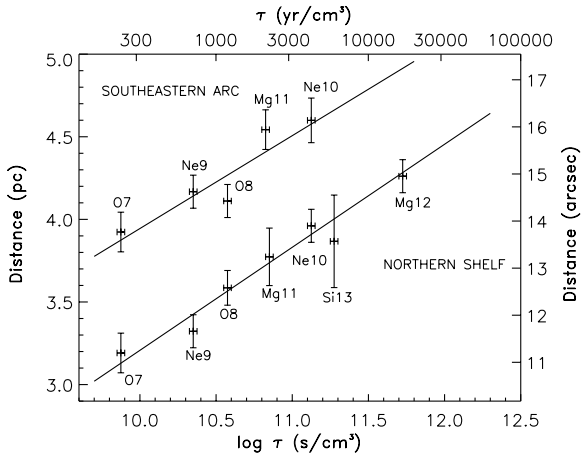

Figure 5. The ionization timescale at peak emissivity plotted against the measured radial distance, for two regions of the SNR depicted in Figure 3. A single electron temperature of 1.14 keV has been assumed (Sasaki, *et al.*[5]). This plot is consistent with an interpretation of progressive ionization structure due to progress of the reverse shock through the ejecta. (Flanagan *et al.*[9])

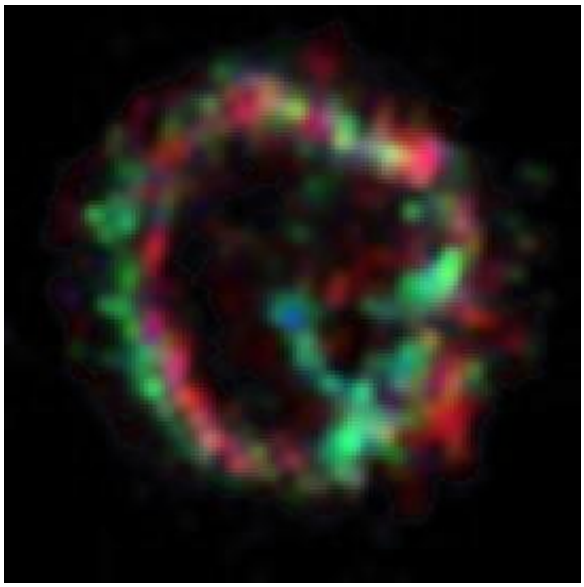

Figure 6. Velocity planes referenced to the zeroth order image are depicted for Ne X Lyman α. Red represents the sum of the two red-shifted planes +1800 km s^{-1} and +900 km $s^{-}1$, green is the -900 km s^{-1} blue-shifted plane, and blue corresponds to the -1800 km s^{-1} blue-shifted plane. (Flanagan *et al.*[9])

We estimated the value of τ as that for which the X-ray emissivity reaches a maximum, assuming a fixed T_e of about 1.14 keV (Sasaki *et al.*[5]) and a plane parallel shock model (Borkowski *et al,*[13]). The radial distance between the edge and the center of the SNR is plotted against τ for seven bright X-ray lines in Figure 5. Measurements are independently plotted for two edges of the SNR: the bright linear "shelf" to the north, and the southeastern arc. (These regions are indicated in Figure 3.) The strong monotonic correlation between radial distance and ionization parameter in Figure 5 supports the interpretation that size differences in the SNR ring are attributable to ionization structure resulting from the reverse shock.

2.3. Two Dimensional Spatial/Velocity Analysis

High velocity motions of bulk matter within the SNR cause Doppler shifts which distort the dispersed images along the dispersion direction. The impact of velocity structure is clearly evident in the *Chandra* HETG spectrum, as shown in Figure 7. The magnitude of these distortions gives a direct measure of the associated velocity. Regions of the SNR along the dispersion direction (east-west) have provided excellent bulk velocity measurements for the individual X-ray lines. Typical red and blue-shifts indicate velocities on the order of 1000 km/s (Flanagan, *et al.*[9,10]), comparable to those of optical filaments.

In order to obtain a more detailed representation of the SNR velocity structure, we have developed a technique that allows us to map the velocity structure on a small (1.5") spatial scale. We begin with a simple model representing the undispersed spectrum. The model is a data cube consisting of two spatial dimensions (a 34X34 array of cells, each of which is 3 ACIS pixels on a side), and a wavelength dimension with Doppler shifts corresponding to five velocities distributed around the rest wavelength of a single X-ray line. (For each velocity plane, the array of cells traces the Ne X Lyman α emission in the undispersed zeroth order image.) The data cube is forward-folded to create modeled images of plus and minus-order dispersed data. In an iterative conjugate gradient scheme, the data cube values are then adjusted to obtain the best fit between the modelled dispersed data and the measured data. The best-fit data cube values have been used to create a color-coded velocity image of the Ne X Lyman α emission (1.022 keV), shown in Figure 6 (Flanagan *et al.*[9]). In this figure,

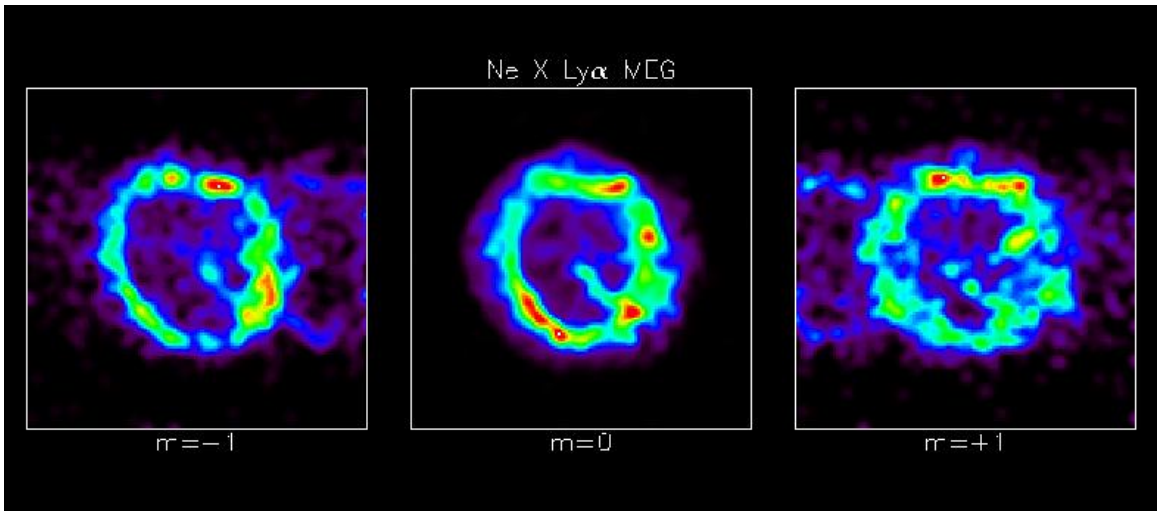

Figure 7. Distortion is evident when dispersed images of NeX Lyman α are compared with the zeroth order (filtered to include only energies around the 1022 eV energy of NeX Lyman α). The leftmost panel shows the MEG -1 order ring, the middle panel is the zeroth order, and the right panel is the MEG +1 order ring. Doppler red shifts in the dispersed images are indicated by distortions outward, away from zeroth order, and blue shifts are indicated by distortions of the ring toward the zeroth order at the center. (Flanagan *et al.*[9])

red represents the sum of two red-shifted velocity planes, while green and blue represent blue-shifted planes. The figure shows a striking east-west offset between red-shifted and blue-shifted emission. This is qualitatively consistent with prelimary modeling of the SNR, which calls for a distribution which is inclined to the line of sight.

2.4. Three Dimensional Physical Model

The unique combination of spatial and spectral resolution obtained with the HETG observation of E0102 has enabled us to pursue a simple qualitative model describing the spatial and velocity distribution of the ejecta. We begin by assuming a spherical shell with a distribution of matter weighted heavily toward the shell's equator and lightly toward the poles. By tilting the inclination so as to match the ellipticity of the E0102 ring, we obtain the limb-brighted appearance seen in *Chandra* images - with a sharp bright shelf to the north, and a bright arc to the south. We further modeled the ejecta as expanding with velocity proportional to radius within the shell (i.e., with the inside of the shell moving outward at 1400 km/s, and the outside moving at 1800 km/s.) Finally, in order to accomodate the steep edge profile, the emission was given a radial power law dependence. This model reproduces many of the features of the HETG spectrum, including intriguing systematic differences between the +1 and -1 orders throughout the dispersed spectrum. It is in reasonable agreement with the spatial distribution found by Hughes *et al.*[14]. It fails to account, however, for the striking separation of Doppler shifted components seen in Figure 6. Other distributions make a better match with the Doppler map, but must satisfy the constraints of the edge profile modeling. This working model will serve as a departure point for future modeling.

3. SS433 JETS

The Galactic X-ray binary SS433 is a source known to have both red and blue shifted lines of the H Balmer series (Margon *et al.*[15]). These lines have been interpreted as emission from opposing jets in the vicinity of the compact object. This kinematic model assigns a jet velocity 0.260c which precesses with a 162.5 day period about an axis inclined to the line of sight. Assuming uniform outward flow, the widths of the optical lines indicate that the full opening angle of the jet is about 5°. Radio jets have been detected (Hjellming *et*

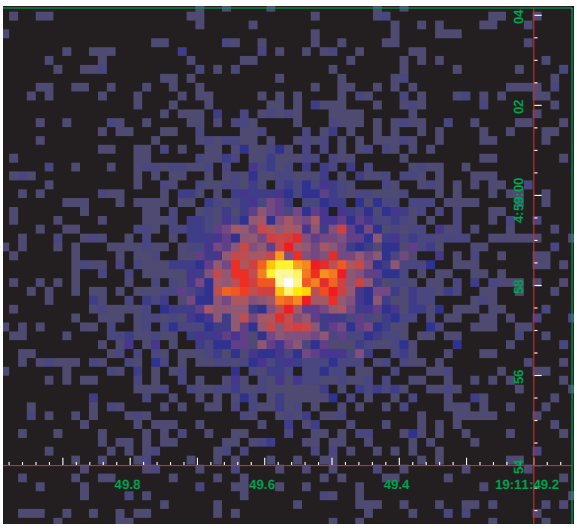

Figure 8. Zeroth-order (undispersed) image of SS433. Although heavily piled up, the elongating in the east-west direction is real, similar in direction and extent to radio jets. (Marshall *et al.*[19])

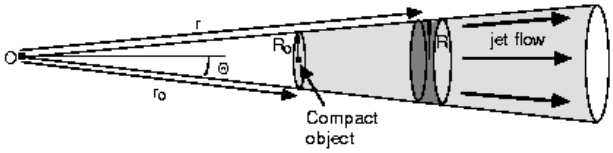

Figure 9. The X-ray spectrum of the SS433 jet is compatible a diverging cone of material in free expansion. The opening angle is defined to be twice Θ. (Marshall *et al.*[19])

al.[16]) extending to arcescond scales, having a corkscrew appearance due to precession. The X-ray source is eclipsed with a 13.1 day period, and a 6.7 keV line appears to shift with the precession phase (Watson *et al.*[17]). Subsequent observations have led to the conclusion (Kotani *et al.*[18]) that the redward jet is obscured by neutral material in an accretion disk. SS433 was observed with the *Chandra* HETGS on September 23, 1999. Below are highlighted some of the results obtained from the high-resolution X-ray spectrum. Further details are given by Marshall *et al.*[19].

The zeroth-order image of SS433 is given in Figure 8. Although the count rate was high and it was heavily "piled-up", detailed analysis of the zeroth order image showed a distinct elongation in the east-west direction. The orientation and extent of this emission corresponds with the arcsecond scale radio jet.

3.1. Doppler Shifts and Broadening – Velocity and Cone Angle

The HETGS X-ray spectrum is shown in Figure 10, where the HEG and MEG data are combined. Cursory inspection of the spectrum reveals several features. Many broad emission lines can be seen atop a significant coninuum level. Some of these lines are identified in the figure. The broad range of ionization states (up to hydrogen-like iron!) indicates a wide range of temperatures. Red and blue-shifted components are detected clearly for the stronger lines. All of these Doppler shifts are compatible with a *single jet speed*. Thus the jets are expanding freely. The measured Doppler shifts of the blue and red jets yield $\beta = v_j/c = 0.2669 \pm 0.0007$, larger than found for the Hα lines by 2920 $\pm$ 440 km s^{-1}.

Measurement of the line widths were similarly consistent with a single value: FWHM=1710 $\pm$ 80 km s^{-1}. This is ascribed to Doppler broadening from the divergence of a cone of outflowing material (Begelman *et al.*[20]). A diagram of this diverging cone is shown in Figure 9. Under this assumption, the full opening angle of the cone (i.e., twice the angle Θ in Figure 9) is 1.23 $\pm$0.06°, much smaller than the 5° full cone angle found for the optical lines. The difference in cone angle and velocity suggests that the optical and X-ray emitting regions may be physically distinct. They're also at different temperatures by a factor of ∼1000!

3.2. Plasma Diagnostics – Adiabatic Cooling

Using the ratio of H-like to He-like line fluxes and assuming collisional ionization equilibrium, it was determined that a broad range of temperatures is needed (1–10 keV) to model the X-ray emission. A satisfactory fit was

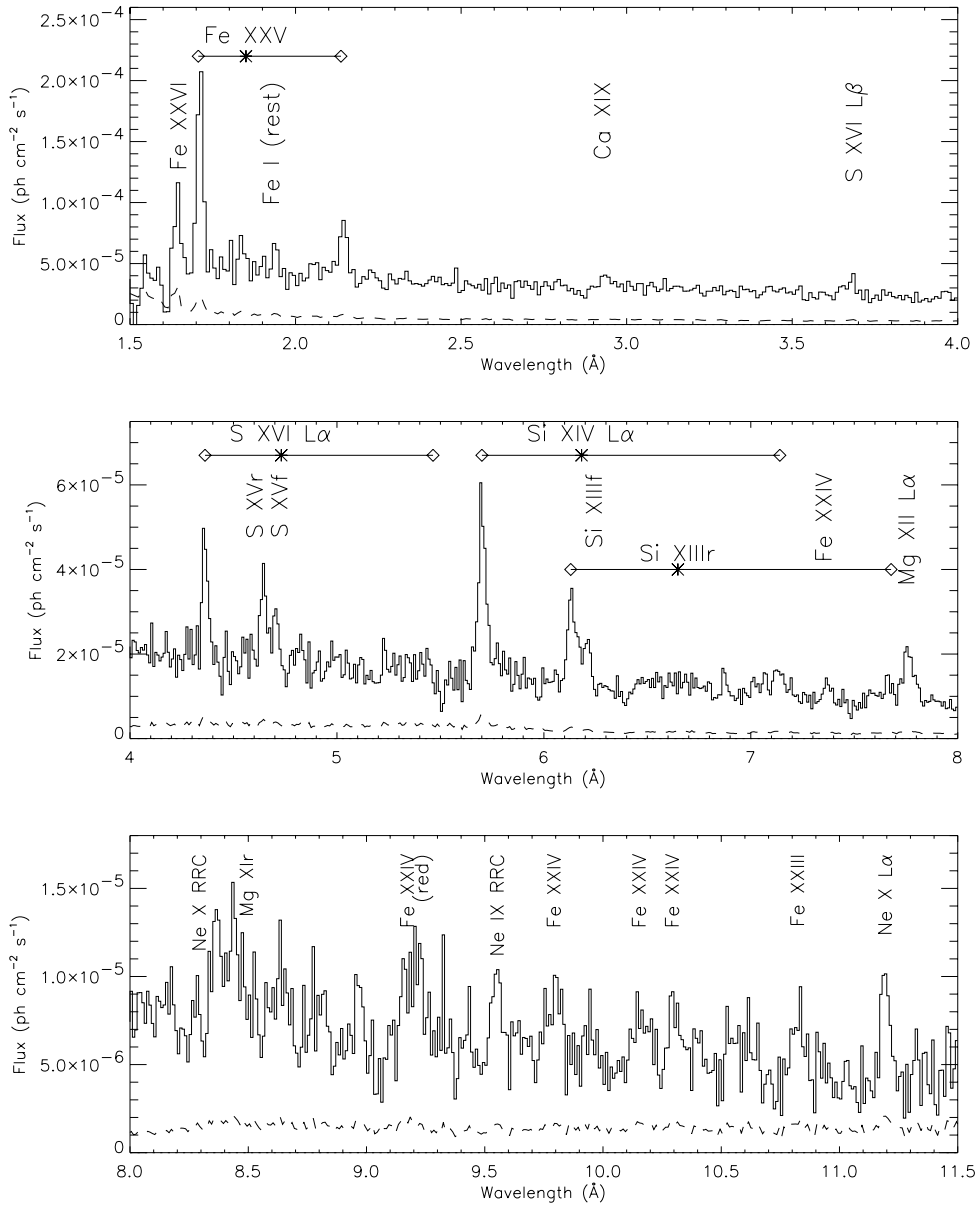

Figure 10. HETG spectrum of SS433; HEG and MEG data are combined at the MEG resolution. Horizontal lines connect the blue and redshifted lines (indicated by diamonds) to the rest wavelengths (asterisks). (Marshall *et al.*[19])

obtained to the complete set of blue-shifted lines with four temperature components, and enhanced abundances of Fe, S, Si and Mg relative to solar. The set of red jet lines required a two-component model. The models for the red and blue jets are shown in Figure 11, overlaid on the HEG data. The model is in reasonably good agreement with the data.

In principle, the four components that make up the fit to the blue-shifted lines provide a set of four temperatures and four emission measures associated with these temperatures. For uniform outflow at constant velocity, the density follows $n \propto r^{-2}$. For adiabatic cooling, $T \propto r^{-4/3}$ for $r \gg R_0/\Theta$, where R_0 is the radius of the jet base. Relating this to emission measure (EM), we find $EM(T) \propto n^2 r^3 \propto T^{3/4}$. Figure 12 displays the best

fit temperatures and emission measures, overlaid with the expected relation for adiabatic expanding uniform outflow. The correspondence is good – the deviation of the last point may be explained by increased optical thickness or truncation of the jet. Thus, the emission measures and temperatures of these four components were found to agree well with adiabatic cooling of a freely expanding jet.

Fits to the blue Si XIII triplet lines were used to determine the density sensitive line ratio $R(n_e) = f/i$, where f and i are the fluxes of the forbidden and intercombination lines. The result gives $n_e \sim 10^{14}$ cm^{-3}. Since the Si XIII emission is dominated by gas close to the temperature of one of the four fitted components, this value of the electron density was assigned to that component. Substitution of n_e into the emission measure then yields the radius, r=1.22×10^{11}. If one assumes the relation for adiabatic expansion, the remaining three temperature components can be determined. The results, summarized in Table 1, indicate that the temperature drops by a factor of 20 while the density drops by a factor of 50 along the jet. From the measured jet velocity, the mass outflow is calculated to be 1.5×10^{-7} M$_\odot$yr^{-1}. This is equivalent to a kinetic energy 1000 times larger than the jet X-ray luminosity from 2–10 kev!

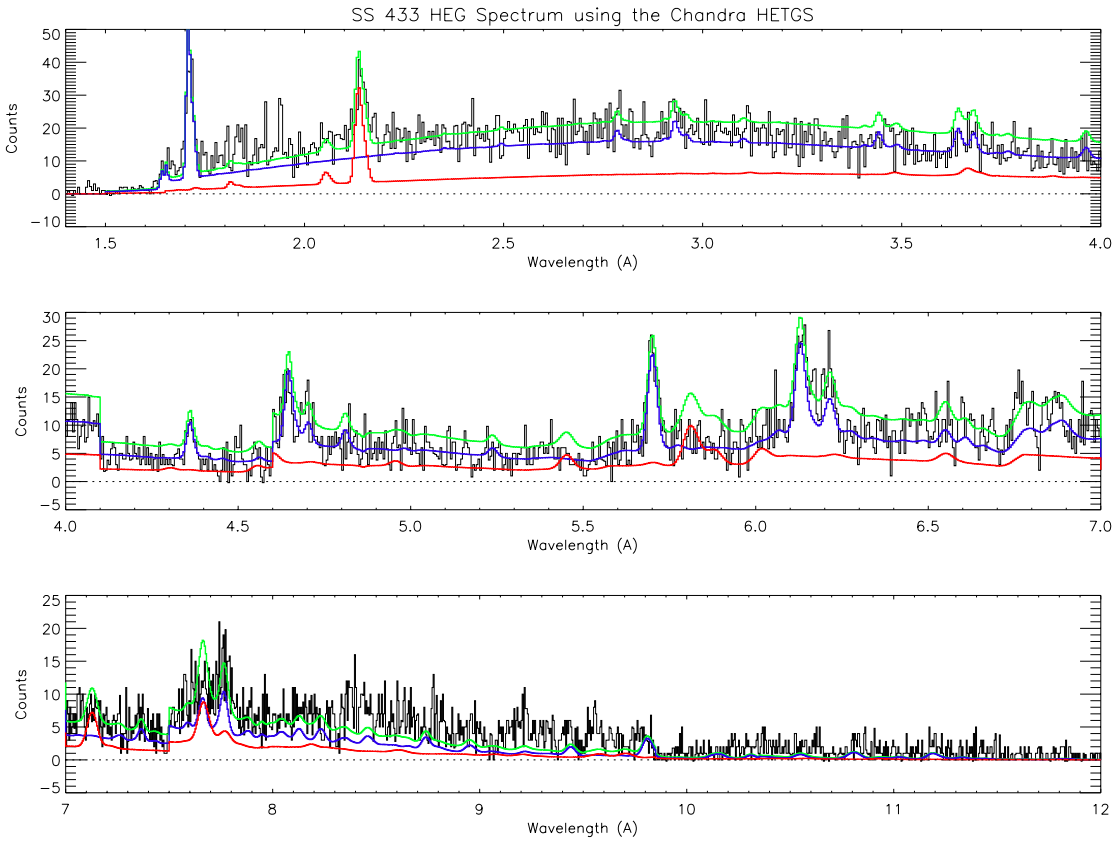

Figure 11. The HEG spectrum compared with models of the spectra of the red and blue jets. The sum of the red and blue jet models is also shown. (Adapted from Marshall *et al.*[19])

4. MICROQUASAR: GRS1915+105

The Galactic X-ray transient GRS 1915+105 with a luminosity of up to few $\times10^{39}$ erg s^{-1} is among the most energetic objects in our Galaxy, showing repeated flares and temporal variations $\gtrsim$ two orders of magnitude. The donor of this binary is believed to be a K-M III giant (Greiner *et al.*[21]), whose kinematics point to a black hole companion of 14 M$_\odot$. One of the most remarkable aspects of this system is that X-ray flares are sometimes

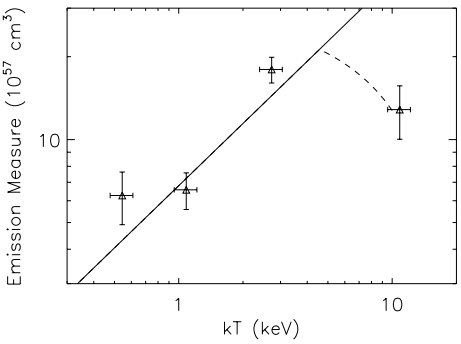

Figure 12. Emission measure vs temperature for the four-component fit to the blue jet lines. The line indicates the expected relation for adiabatic expansion. (Marshall *et al.*[19])

r_0 ($\times 10^{10}$cm)	2	6	12	20
T ($\times 10^6$K)	126	32	13	6
n_e ($\times 10^{13}$cm^{-3})	186	47	10	4

Table 1. Temperature T and density n_e vary as a function of position along the jet. Approximate values have been taken from Marshall *et al.*[19]

followed by superluminal ejection events which show jet velocities (as inferred from radio maps) up to $v \sim 0.95c$ (i.e. a Lorentz factor of 3). (Less energetic persistent radio emission are found to be present during the low-hard state.)

Because of the many similarities between radio-loud AGNs and GRS 1915+105 (and other binaries like it), these energetic Galactic sources are commonly referred to as "microquasars". As the Galactic analogues of AGN, there are several advantages to studying them. In particular, because of their proximity to us and smaller size, these sources are much brighter, and have characteristic timescales which are much shorter than their extragalactic counterparts making study less costly. As such, these objects may be key to providing the unique laboratory for thoroughly examining the generic physics underlying all accretion systems.

Here, we detail highlights from the *Chandra* HETGS and simultaneous *RXTE* Proportional Counter Array (PCA) observations of GRS 1915+105 on April 24, 2000. Details can be found in Lee *et al.*[22].

4.1. Neutral Edges - Anomalous Abundances and EXAFS?

Prominent K-shell absorption edges of neutral Fe, S, Si and Mg were detected in the high-resolution HETG spectrum (Figures 13, 14) of GRS 1915+105. The discontinuity at the Mg and S edges indicate column densities which are consistent with that expected from neutral line-of-sight absorption. This is contrasted with the column densities derived from Fe and Si which reveal anomalous abundances, suggesting additional iron and silicon-enriched cold absorbing material which may be intrinsic to the source. (Note for example the remarkable prominence of the Si edge relative to the Mg and S edges in Figure 13). The presence of enhanced Fe and Si may provide clues to the evolution of this source and the black hole in particular, but further study is needed.

A potentially exciting discovery is that of XAFS (X-ray Absorption Fine Structure), most notable near the photoelectric edge of Si. Such features appear as wave-like modulations near the edge (see Figure 13, middle panel). If confirmed, this would be the first astrophysical detection of XAFS, indicating a direct detection of absorption by material in solids (e.g. interstellar grains).

4.2. Ionized Absorption Lines - Variation of FeXXV and Fe XXVI

In addition to neutral edges, spectral features in the form of hydrogen– and helium–like Fe (XXV, XXVI) resonant absorption was found in the HETG spectrum of GRS 1915+105. (This combination of neutral and ionized spectral features is seen nicely in the 30 ks time-integrated spectrum of Figure 14.) These high ionization absorption lines indicate a very hot environment, which must be distinct from the region where the cold edges originate. Assuming photoionization and a Γ=2 power law ionizing spectrum, the emitting region and the absorber are calculated to be within $\lesssim 2\times10^{11}$ cm of each other. Accordingly, it is likely that the material giving rise to the high ionization lines are associated with the accretion disk atmosphere/corona/wind.

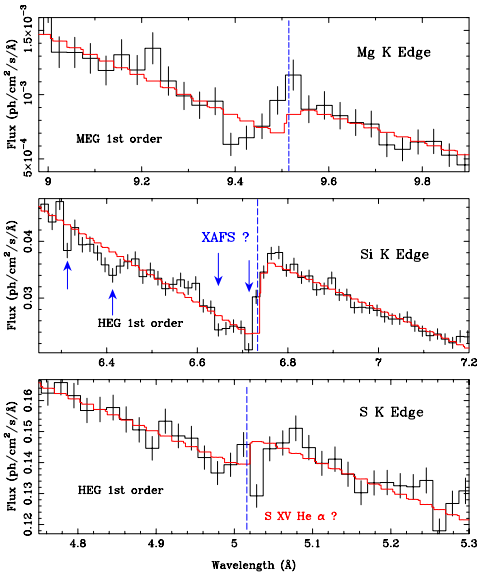

Figure 13. Photoelectric K-shell edges of Mg, Si and S. Note the prominence of the Si edge, and possible EXAFS structure. (Lee *et al.*[22])

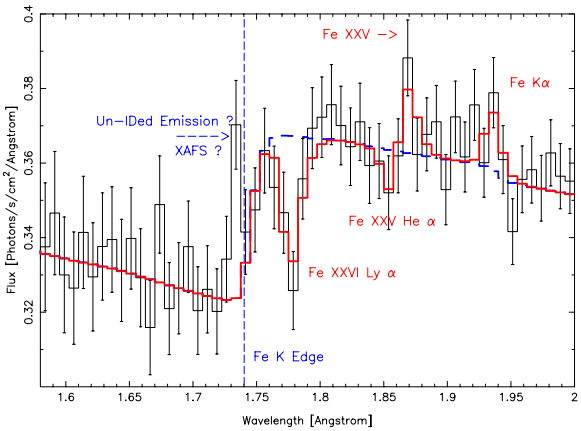

Figure 14. The Fe K edge is shown where ionized hydrogen-like Fe XXVI and helium-like Fe XXV are also seen. Overplotted are the best-fit continuum (dashed) and identified (solid) lines. (Lee *et al.*[22])

During the 2000 April observation, the X-ray flux of GRS 1915+105 was found to vary by $\sim$ 20 % on a timescale of $\sim$ 10 ks (Figure 15). The *RXTE* and *Chandra* light curves coincide in phase, as expected, along with the blackbody and power law components of the broadband RXTE spectrum. To assess spectral variability in detail, the high-resolution HETG spectrum was partitioned in three distinct 10 ks phases, corresponding to periods when the light curve count rate was highest (top and bottom panels of Figure 16, respectively 0-10 ks and 20-30 ks), and when it was low (middle panel, 10-20 ks). As can be seen, the ionized absorption lines evolve on $\sim$ 10 ks timescales, with Fe XXVI absorption being most pronounced during the peaks in the light curve, but weak during the trough. This is contrasted with the Fe XXV absorption which is most pronounced during the count rate minimum, while virtually disappearing during the light curve maxima. Assuming that the ionization parameter ξ scales with flux, while the number density of electrons and the distance between the ionizing source and absorber remain constant in this region, the observed spectral changes can be partly attributed to changes in the ionizing flux. However, the 20 % change observed in flux implies an $\sim$ 30 % change in the ionization fraction of Fe XXV – this is insufficient to explain the lack of Fe XXV and dominance of Fe XXVI during the beginning and end periods corresponding to high count rate. Accordingly, changing density may also be a factor, such that spectral variability may be indicative of a flow which can change on timescales of $\sim$ 10 ks. This is not inconceivable since 10 ks is a very long time, corresponding to many dynamical timescales of the relevant parts of the disk, in the life of a source like GRS 1915+105.

5. SUMMARY

The HETG spectra we have examined in these three examples illustrate the kinds of science made possible by high spatial and spectral resolution. The HETGS observation of the supernova remnant E0102-72 has provided evidence of the reverse shock through the ejecta, constraints on the temperature and ionization age, and a detailed two-dimensional Doppler map of the entire remnant. This has led to the next obvious step of modeling the remnant in three dimensions. The HETGS observation of SS433 reveals jets in free expansion at a velocity of 0.2699c. The jets can be modeled as uniform outflow through a cone of opening angle 1.22 degrees, undergoing adiabatic cooling. The picture we have is a jet whose temperature and density drop steeply with distance, and whose kinetic energy dominates the measured X-ray luminosity by a factor of a thousand! These examples show us what can be learned from emission lines, but absorption features can be equally revealing. For instance, the

HETG spectrum of GRS 1915+105 has uncovered anomalous Fe and Si abundances in cold material which may be intrinsic to the source, as well as highly ionized hydrogen-like and helium-like Fe which likely originate in the accretion disk atmosphere. Spectral variability studies of this source point to the possibility of a slow outflow. The detection of XAFS if confirmed would be the first direct probe of the inner structure of interstellar dust grains.

These three observations are representative samples of the science returned by the HETGS in the first three years of *Chandra's* operation. With majority of the mission still ahead, there is every reason to hope that these examples will be "typical" of *Chandra's* future.

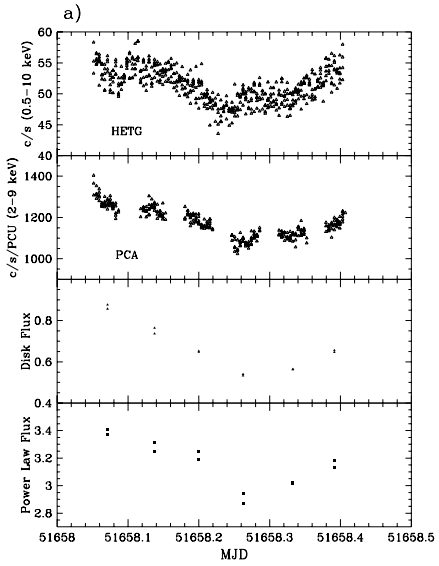

Figure 15. The *Chandra* and RXTE light curves spanning ∼30 ks on April 24, 2000. The broad-band spectra detected by RXTE are seen to change for both the blackbody and power-law components. (Lee *et al.*[22])

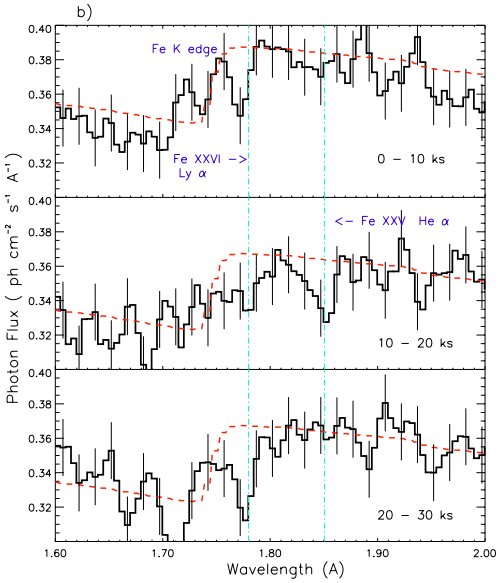

Figure 16. The 30 ks *Chandra* spectrum is divided into 10 ks intervals. The first and third panels correspond to the peak flux periods when the hydrogen-like Fe XXVI Lyman α absorption is prominent and the helium-like Fe XXV He α is absent. In the middle panel, when the light curve count rate is at a minimum, the situation is reversed: the Fe XXV absorption is now prominent while the Fe XXVI is less so. (Lee *et al.*[22])

5.1. Acknowledgments

We thank the HETG/CXC team for helpful discussions. We are grateful to Stephen Murray for help in preparing the "plasma movie" illustrating the evolution of a remnant after passage of a shock. We are grateful to Alexey Vikhlinin for his latex expertise. This work was prepared under NASA contracts NAS8-38249, NAS8-01129, and NAS8-39073 and SAO SV1-61010.

REFERENCES

1. Markert, T.H., Canizares, C.R., Dewey, D., McGuirk, M., Pak, C., and Schattenburg, M.L. 1994, SPIE Proceedings, 2280, 181
2. Chandra Proposers' Observatory Guide, Version 4.0, 2001, `http://cxc.harvard.edu/udocs/docs/docs.html`
3. Gaetz, T.J., Butt, Y.M., Edgar, R.J., Eriksen, K.A., Plucinsky, P.P., Schlegel, E.M. and Smith, R.K. 2000, ApJ, 534, L47

4. Hayashi, I., Koyama, K., Masanobu, O., Miyata, E., Tsunemi, H., Hughes, J.P. and Petre, R. 1994, PASJ, 46, L121
5. Sasaki, M., Stadlbauer, T.F.X., Haberl, F., Filipovic, M.D. and Bennie, P.J. 2001, A&A, 365, L237
6. Rasmussen, A.P., Behar, E., Kahn, S.M., den Herder, J.W. and van der Heyden, K. 2001, A&A, 365, L231
7. Canizares, C.R., Huenemoerder, D.P., Davis, D.S., Dewey, D., Flanagan, K.A., Houck, J., Markert, T.H., Marshall, H.L., Schattenburg, M.L., Schulz, N.S., Wise, M., Drake, J.J. and Brickhouse, N.S. 2000, ApJ, 539, L41
8. Canizares, C.R., *et al.* 2002, in preparation.
9. Flanagan, K.A., Canizares, C.R., Davis, D.S., Dewey, D., Fredericks, A.C., Houck, J.C., Markert, T.H., and Schattenburg, M.L. 2002, in prep.
10. Flanagan, K.A., Canizares, C.R., Davis, D.S., Dewey, D., Houck, J.C., Markert, T.H. and Schattenburg, M.L in X-Ray Astronomy 2000, ASP Conference Proceeding Vol. 234, Serio and Giacconi eds. 2001
11. Flanagan, K.A., Canizares, C.R., Davis, D.S., Houck, J.C., Markert, T.H., and Schattenburg, M.L. 2001, *Young Supernova Remnants: Eleventh Astrophysics Conference, College Park, Maryland 2000* (AIP Conference Proceedings vol 565: New York), eds. S. S. Holt and U. Hwang
12. Canizares, C.R., Flanagan, K.A., Davis, D.S., Dewey, D. and Houck, J.C. in X-Ray Astronomy 2000, ASP Conference Proceeding Vol.234, Serio and Giacconi eds. 2001, p.173
13. Borkowski, K.J., Lyerly, W.J. and Reynolds, S.P. 2001, ApJ, 548, 820
14. Hughes, J.P. 1988, in Supernova Remnants and the Interstellar Medium, ed. R.S. Roger and T.L. Landecker (Cambridge: Cambridge Univ. Press), 125
15. Margon, B., Ford, H.C., Katz, J.I., Kwitter, k.B., Ulrich, R.K., Stone, R.P.S. and Klemola,A. 1979, ApJ, 230, L41
16. Hjellming, R. and Johnston, S. 1981, ApJ, 246, L141
17. Watson, M.G., Stewart, G.C., Brinkmann, W. and King, A.R. 1986, MNRAS, 222, 261
18. Kotani, T., Kawai, N., Matsuoka, M. and Brinkmann, W. 1996, PASJ, 48, 619
19. Marshall, H.L., Canizares, C.R. and Schulz, N.S. 2002, ApJ, 564, 941
20. Begelman, M.C., Sarazin, C.L., Hatchett, S.P., McKee, C.F. and Arons, J. 1980, ApJ, 238, 722
21. Greiner, J., Cuby, J.G., McCaughrean, M.J., Castro-Tirado, A.J. and Mennickent, R.E. 2001, A&A, 373, L37
22. Lee, J.C., Reynolds, C.S., Remillard, R., Schultz, N.S., Blackman, E.G. and Fabian, A.C. 2002, ApJ, 567, 1102